

# In Situ Atomic Force Microscopy Analysis of the Corrosion Processes at the Buried Interface of an Epoxy-like Model Organic Film and AA2024-T3 Aluminum Alloy

Ahed Almalla, Ozlem Ozcan,\* and Julia Witt

The application of characterization methods with high spatial resolution to the analysis of buried coating/metal interfaces requires the design and use of model systems. Herein, an epoxy-like thin film is used as a model coating resembling the epoxy-based coatings and adhesives widely used in technical applications. Spin coating is used for the deposition of a 30 nm-thin bilayer (BL) composed of poly(ethylenimine) (PEI) and poly[(*o*-cresyl glycidyl ether)-*co*-formaldehyde] (CNER). Fourier-transform infrared spectroscopy (FTIR) results confirm that the exposure of coated AA2024-T3 (AA) samples to the corrosive electrolyte solution does not cause the degradation of the polymer layer. In situ atomic force microscopy (AFM) studies are performed to monitor local corrosion processes at the buried interface of the epoxy-like film and the AA2024-T3 aluminum alloy surface in an aqueous electrolyte solution. Hydrogen evolution due to the reduction of water as the cathodic corrosion reaction leads to local blister formation. Based on the results of the complementary energy-dispersive X-ray spectroscopy (EDX) analysis performed at the same region of interest, most of the hydrogen evolved originates at the vicinity of Mg-containing intermetallic particles.

However, compositional differences of the IMPs (IMPs) and the resulting differences in their nobility lead to a high susceptibility to galvanic corrosion.<sup>[2]</sup> Buchheit et al. determined the corrosion potential of different intermetallic phases on Al-alloy model bulk samples using standard electrochemical techniques.<sup>[2c]</sup> The measured corrosion potentials were representative of the behavior of IMPs and provided important information for the understanding of their galvanic role relative to the Al matrix. Furthermore, Buchheit et al.<sup>[2a]</sup> reported that 60% of the IMPs were S-phase (Al<sub>2</sub>CuMg), and the rest were AlCuFeMn IMPs with a range of compositions including Al<sub>7</sub>CuFe<sub>2</sub>, Al<sub>6</sub>MnFe<sub>2</sub>, (Al,Cu)<sub>6</sub>Mn, and a number of undetermined compositions in the class Al<sub>6</sub>(Cu,Fe,Mn). The role of IMPs on the corrosion behavior of uncoated AA2024-T3 in aqueous solutions containing aggressive chemical species such as chloride-containing media is well documented in the literature.<sup>[2e,3]</sup> The application of

## 1. Introduction


The aluminum alloy AA2024-T3 is an important material for aerospace applications due to its high strength-to-weight ratio. The alloy constituents Cu, Fe, Mn, and Mg result in microstructural heterogeneity by formation of intermetallic particles (IMPs), thereby improving the mechanical properties significantly.<sup>[1]</sup>

high-resolution techniques aiming at a better mechanistic understanding of the localized corrosion activity on AA2024-T3 on the nanometer scale is demonstrated by many research groups.<sup>[2d,4]</sup>

Atomic force microscopy (AFM) is one of the most prevailing methods for in situ analysis of morphological changes during electrochemical processes in aqueous environments. This technique provided considerable understanding of the corrosion behavior of AA2024-T3. Leblanc and Frankel developed a micro-masking method, which allowed the investigation of microstructural elements at a smaller scale than  $2 \times 2 \mu\text{m}$ . Their results demonstrated that the noble Al–Cu–(Fe, Mn) inclusions have a cathodic character initiating pitting corrosion when large electrode areas are exposed to an electrolyte. However, as the area ratio of these particles to its surrounding increases, and the mechanism of pitting corrosion changes from the dissolution of the S-phase particles to an attack of the Al matrix. If the micro-masked area contains only the Al–Cu–(Fe, Mn) IMPs, the corrosive attack is observed.<sup>[5]</sup> Recent studies by means of transmission electron microscopy (TEM) contributed significantly to our understanding of the different IMPs' role on the corrosion initiation on the bare AA2024-T3 surface.<sup>[2d,4e–g]</sup> The main consensus of these studies is that the dealloying of various IMPs is the key factor controlling the localized corrosive attack and the kinetics of selective dissolution/redistribution of

A. Almalla, O. Ozcan, J. Witt  
Interfacial Processes and Corrosion  
Bundesanstalt für Materialforschung und -prüfung (BAM)  
12205 Berlin, Germany  
E-mail: ozlem.ozcan@bam.de

A. Almalla  
Organic Chemistry  
Freie Universität Berlin  
14195 Berlin, Germany

 The ORCID identification number(s) for the author(s) of this article can be found under <https://doi.org/10.1002/adem.202101342>.

© 2022 The Authors. Advanced Engineering Materials published by Wiley-VCH GmbH. This is an open access article under the terms of the Creative Commons Attribution License, which permits use, distribution and reproduction in any medium, provided the original work is properly cited.

DOI: 10.1002/adem.202101342

IMP constituents, as well as the microstructural characteristics of the IMPs also play a major role. Moreover, inhomogeneities within the IMPs as well as the interfaces between IMPs and the surrounding matrix result in galvanic coupling effects at the nano- or even atomic scale.<sup>[4e,g]</sup> It is reported by Wang et al. that S-phase IMPs containing Al<sub>20</sub>Cu<sub>2</sub>Mn<sub>3</sub> inclusions show much higher anodic activity than those free of such dispersoids in experiments on bare aluminum alloy surfaces.<sup>[4f]</sup> Wang et al. reported that the S-phase particle and the Al<sub>20</sub>Cu<sub>2</sub>Mn<sub>3</sub> dispersoids take the anodic role and are supported by the surrounding matrix as the cathode. In their liquid-phase TEM (LP-TEM) study, Kosari et al. investigated in situ the dissolution of the S-phase IMPs on a bare AA2024-T3 substrate in a 0.01 M NaCl electrolyte. The kinetics of trench formation and Cu dealloying were observed at a very early stage at around 19 and 21 min, respectively.

When the alloy surface is coated with an organic film during exposure to a corrosive electrolyte, the characteristics of the local corrosive environment in the buried interface and the resulting corrosion mechanisms differ drastically from the scenario of the bare alloy surface. The application of analytical tools with high spatial or spectral resolution requires a careful design of model systems.<sup>[6]</sup> A unique advantage of AFM is that, when operated in the scanning Kelvin probe force microscopy (SKPFM) mode, it can provide information from buried polymer/metal interfaces to visualize corrosion-induced delamination processes at polymer-coated metal surfaces with a high spatial resolution.<sup>[6a,b,7]</sup> Even though it was demonstrated that filiform corrosion can still be monitored under a 500 nm-thick polymer film,<sup>[7]</sup> ideally, the applied coating has to have a smooth surface and a film thickness below 100 nm to guarantee a high spatial resolution and a potential signal free of topography-induced artifacts.<sup>[6a,8]</sup> In their pioneering work, Senoz and Rohwerder clearly demonstrated that the IMPs at the immediate vicinity of the active head determine the progress of filiform corrosion.<sup>[6a]</sup> They reported that the anodic head of the filigree pulls down the electrode potential at the intact interface, also for cathodic IMPs, which can lead to cathodic delamination. The resulting pressure build-up in the active head is reported to trigger an abrupt coating delamination and the progress of the active head to a new position.<sup>[6a]</sup> In a further study, Senoz et al. refined this observation and presented the activity of the IMPs at the vicinity of the filiform head as the main factor determining the filiform growth.<sup>[7]</sup>

In this study, model thin films mimicking the technical epoxy–amine systems were used to investigate the local corrosion processes during immersion conditions in a 0.1 M solidum perchlorate electrolyte. Using ex situ correlative energy-dispersive X-ray spectroscopy (EDX) analysis, we were able to locate the hydrogen evolution at the buried interface, which may play an important role in the detachment of the organic coating during the delamination processes.

## 2. Results and Discussion

### 2.1. Corrosion of Bare AA2024-T3

In situ AFM corrosion experiments on bare substrates were performed in a 0.1 M NaClO<sub>4</sub> electrolyte solution for a duration of

4 h. In **Figure 1**, the AFM topography image and the Volta potential map of an AA sample before and after the in situ AFM corrosion experiment are presented. The raised features seen in the topography image (Figure 1a, left) are associated with IMPs. These particles were clearly identified by the Volta potential map (Figure 1a, right). Particles labeled B showed the highest Volta potential and can be ascribed as AlCuFeMn-containing particles, while the particle labeled A was identified as S-phase (Al<sub>2</sub>CuMg) particle due to its lower potential.

Due to the low nobility and high reactivity of Mg, particle A immediately started to dissolve when it came in contact with the electrolyte solution (Figure 1b, left). Fe-containing particles remained inside the Al matrix. These particles exhibited a low tendency to dissolve in electrolyte due to their high nobility. In comparison with the fast dissolution activities associated with Mg-rich particles,<sup>[2d]</sup> there were only little changes observed in the topography of the Fe-containing particles B, while the SKPFM measurements revealed a decrease in the Volta potential difference between the Fe-containing particles and the Al matrix (Figure 1b, right). This was comparable with the results obtained on coated AA samples. However, Mg-containing particle A shows a clearly higher potential than before corrosion. This can be explained by the preferential dissolution of Mg, which led to enrichment of copper and caused oxide coverage around the attack region, causing the increase in Volta potential after corrosion.

**Figure 2** presents the SEM image and the corresponding EDX elemental maps acquired at the same area as the AFM topography image in Figure 1b on bare AA after corrosion in 0.1 M NaClO<sub>4</sub> electrolyte solution over 4 h. The EDX maps indicate the presence of b) C, c) O, d) Fe, e) Cu, f) Mn, g) Al, and h) Mg. The SEM images confirmed the formation of small pits. The undissolved particles labeled B contained Fe, Cu, and Mn. The particle labeled A was assigned as S-phase particle. EDX analysis confirmed the enrichment of copper and formation of copper oxide during the corrosion of the S-phase particle (Figure 2c,e). It has to be noted that, in the absence of a coating, it can never be avoided that soluble corrosion products are rinsed from the surface during sample preparation for electron microscopy.

### 2.2. Corrosion of AA2024-T3 Coated with a Thin Epoxy-like Polymer Film

The spin-coating technique was used for the deposition of a 30 nm-thin bilayer (BL) consisting of a poly-(ethylenimine) (PEI) on the top of the AA2024-T3 aluminum alloy (AA) sample and a final poly[(*o*-cresyl glycidyl ether)-*co*-formaldehyde] (CNER) layer. This sample is denoted as (CNER/PEI)<sub>1</sub>/AA. The preparation and full characterization of the model film system has been presented and discussed in a previous publication.<sup>[9]</sup> The topographical image of the coated sample before the corrosion test is presented in **Figure 3a**. IMPs protrude from the polished sample surface, as they possess a higher hardness and thus a lower polishing rate relative to the matrix. After the deposition of the epoxy-amine BL film, the AFM characterization of the topography indicated a smooth and homogeneous film structure in the surrounding Al matrix. In the SKPFM profiles, the IMPs can be

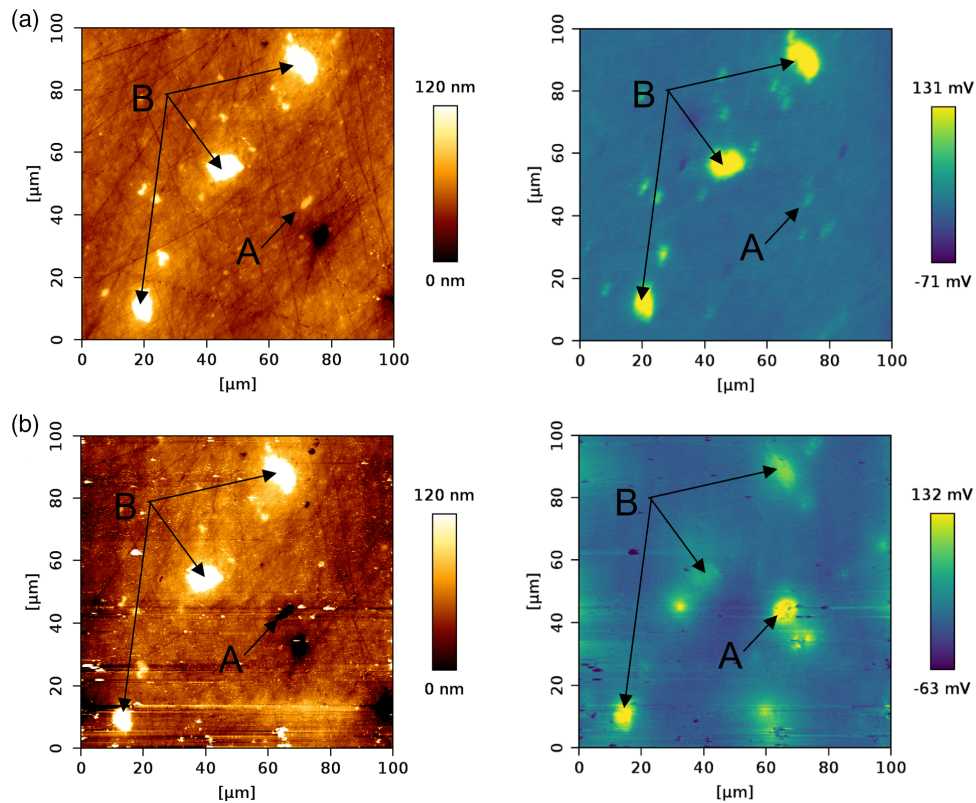


**Figure 1.** AFM topography (left) image and Volta potential map (right) of a bare AA sample a) before and b) after the corrosion experiment in 0.1 M NaClO<sub>4</sub> electrolyte solution.

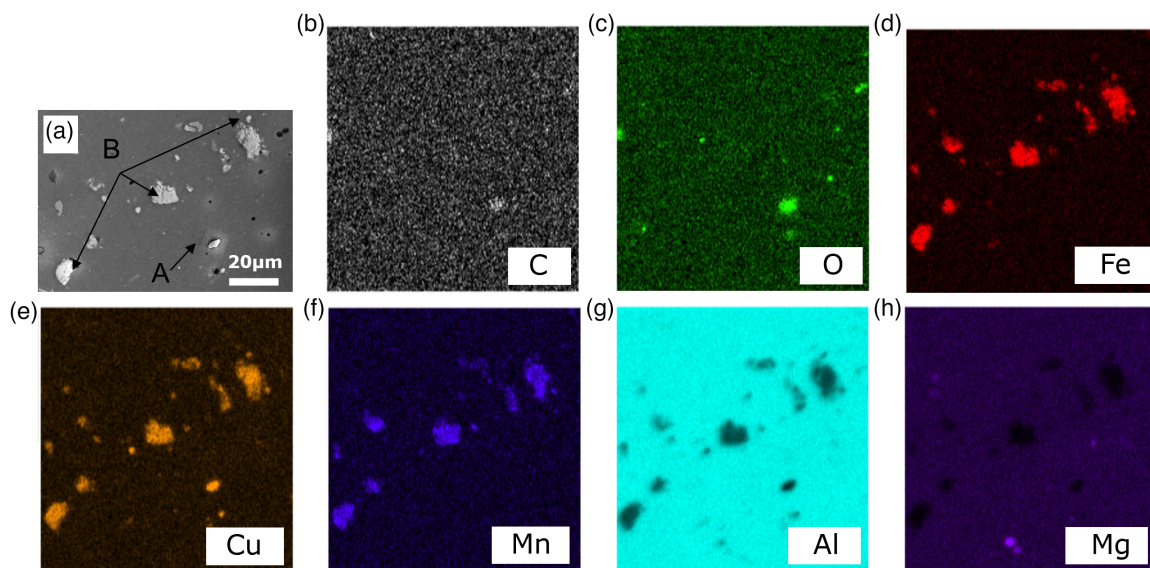


**Figure 2.** a) SEM image recorded in the SE mode and the corresponding EDX analysis showing the presence of b) C, c) O, d) Fe, e) Cu, f) Mn, g) Al, and h) Mg of the same area characterized by AFM.

visualized clearly under the 30 nm thin film. Due to the higher (nobler) Volta potential of the IMPs relative to the Al matrix (Figure 3b), they are expected to act as the initiation sites for localized corrosion. Particles labeled C and D can be ascribed as

AlCuFeMn-containing particles due to the high Volta potential in comparison with particles labeled E, which were identified as Mg-rich S-phase particles (Al<sub>2</sub>CuMg) and exhibit a lower potential than IMPs C and D. This assignment was also confirmed by



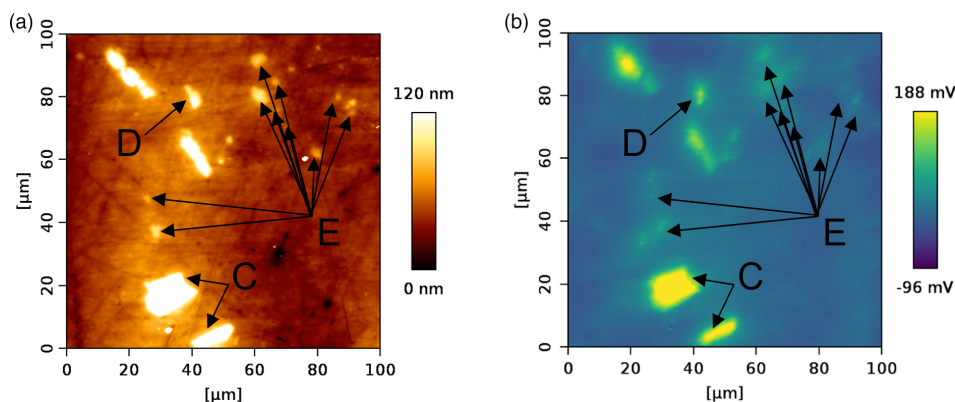


**Figure 3.** a) AFM topography image and b) Volta potential map recorded on a (CNER/PEI)<sub>1</sub>/AA sample before performing in situ AFM corrosion studies.

EDX studies discussed later (Figure 7) and is in good agreement with the SKPFM results published by Schmutz and Frankel.<sup>[4d]</sup> Their study pointed out that the noble nature of Mg-rich particle was caused by the altered surface oxide layer, which is formed on the particles during the polishing procedure in aqueous and even in nonaqueous solutions.

In situ AFM measurements allowed real-time monitoring of the corrosion process at the polymer-coated AA sample in a 0.1 M NaClO<sub>4</sub> electrolyte solution. For in situ imaging, it was necessary to work in the QI mode to minimize tip–sample interactions and avoid tip and sample damage. **Figure 4a** shows the topography of (CNER/PEI)<sub>1</sub>/AA after an immersion time of 7 h. The corresponding section profile in **Figure 4b** illustrates the growth of a blister in height and diameter as a function of time. Blistering can be initiated by the permeation of aqueous electrolyte and oxygen underneath the coating. The cathodic water reduction produces H<sub>2</sub> gas and OH<sup>−</sup> ions, the former leading to pressure build-up and the latter to weakening of adhesive bonds at the polymer/metal interface.

It was evident that blistering immediately started when the coating was brought to contact with the electrolyte (**Figure 4b**, 0 min). The blister that was selected as an example was identified with 1.40 μm maximum height in the AFM topography image recorded directly after adding the electrolyte solution. The height increased after 230 min to 1.95 μm. However, the growth of the blister slowed down, as can be seen from the cross section recorded after 484 min, where the height of the blister was determined as 2.08 μm. The collection of the in situ AFM topography profiles during the corrosion process enabled the analysis of the blister form during growth. The evolution of the blister volume and the surface area of the blister base is presented in **Figure 4c**. After an initial growth phase, the blister base surface area stagnated, while the volume showed a slow increase. In the final phase, both the spreading of the blister at the interface and an increase of the blister volume occurred, probably due to the OH<sup>−</sup>-induced interface degradation and further pressure build-up in the blister.

The subsequent characterization using the QI mode has proved that the polymer layer is free of damage at a large area of 100 × 100 μm (**Figure 5a**). The IMPs were still easily recognizable in the topography image, whereas SKPFM measurements revealed a decrease in the Volta potential difference between

the Fe- and Mg-containing particles and the Al matrix (**Figure 5b**, C, E). In addition, the overall surface potential increased after in situ corrosion experiments, which was also observed on the bare AA sample (**Figure 1**). These changes might result due to the localized dissolution of aluminum around the IMPs and the formation of an aluminum oxide layer.<sup>[10]</sup> Higher Volta potentials were determined for adherent corrosion products (**Figure 5b**, D, spherical agglomerates in the topography). Mg-containing S-phase particles have shown a different corrosion mechanism than observed on bare surfaces (**Figure 1**). Without the epoxy-like model coating, these particles dissolved very quickly. Several authors explained this process by the preferential dissolution of Mg and Al from the S-phase particles Al–Mg–Cu,<sup>[3b,4c,d]</sup> which ultimately leads to the enrichment of copper, in good agreement with our results also to a higher Volta potential (**Figure 1b**, right). The polymer-coated surfaces are apparently protected from the dealloying attack as SKPFM results showed an unchanged topography and no significant increase of the Volta potential at the surface of the S-phase particle relative to the Al matrix (**Figure 5a,b**, particles labeled E).

Besides the characteristic ring-shaped structure in the topography image (**Figure 5a**), a remaining circular pattern (**Figure 5c**) indicated that blisters collapsed upon drying. The fact that the circular pattern was also recognizable in the Volta potential map with areas displaying higher potential values (**Figure 5d**) indicated the formation of corrosion products inside the blisters.

Fourier-transform infrared spectroscopy (FTIR) measurements have been performed to identify the chemical structure of the polymer and to examine the degradative impact of the corrosion on the coated aluminum alloy surface. **Figure 6** shows the spectra measured on (CNER/PEI)<sub>1</sub>/AA directly after preparation and after the sample was exposed to a 0.1 M NaClO<sub>4</sub> electrolyte solution for 7 h. The FTIR spectra of a cured BL on the AA sample reveal characteristic IR absorption modes for PEI and CNER. The IR mode at the wavenumber of 3300 cm<sup>−1</sup> corresponds to the N–H stretching vibrations of secondary amines in PEI, while the absorption mode at 1675 cm<sup>−1</sup> appeared after the curing process and could be associated with the C=O stretching vibration of the primary amide group, which may form due to the interaction of the primary amines with CO<sub>2</sub>.<sup>[11]</sup> According to literature, PEI provides a high CO<sub>2</sub> adsorption capacity, which can lead to the formation of amides after heat treatment below 60 °C.<sup>[12]</sup> The IR



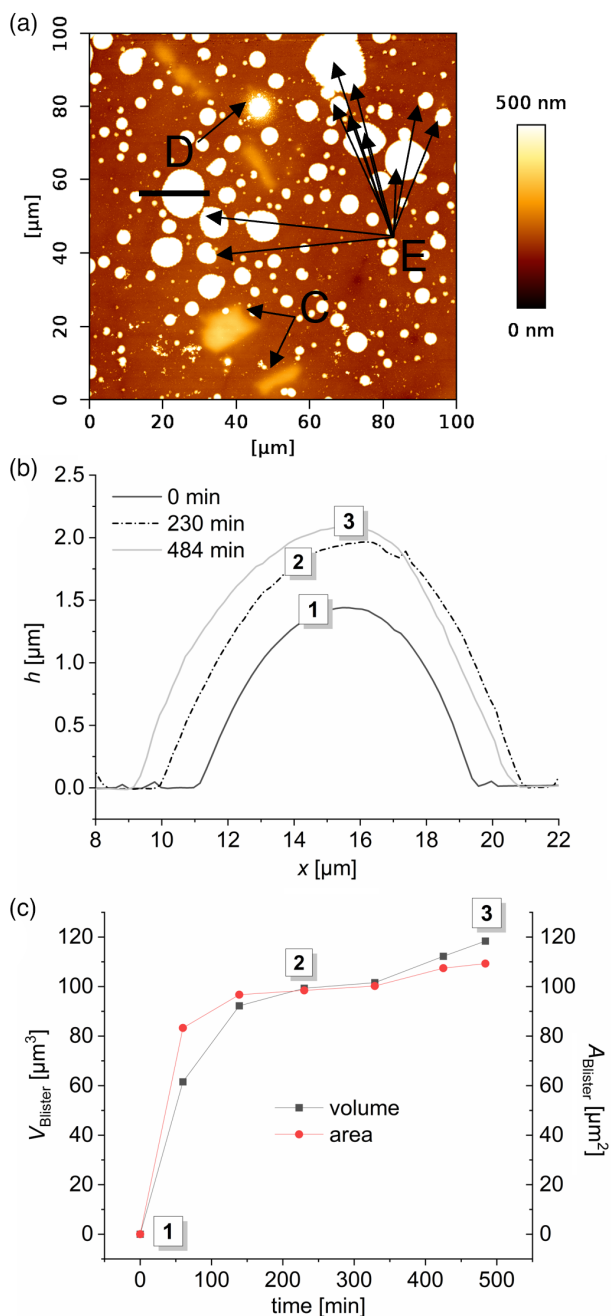


**Figure 4.** AFM topography image acquired during in situ corrosion studies of the same sample surface, as shown in Figure 3, after a) 1 h in a 0.1 M  $\text{NaClO}_4$  solution and b) section profiles illustrating the blister growth after 1 and 7 h of corrosion time. c) The evolution of the blister volume (left axis) and the surface area of the blister base (right axis).

mode at  $1503$  and  $1475\text{ cm}^{-1}$  arose due to C—C and C=C stretching vibrations of the aromatic ring of CNER. FTIR results after the exposure of the sample to a 0.1 M  $\text{NaClO}_4$  electrolyte solution for 7 h indicated the presence of an intact BL as all characteristic peaks for PEI and CNER were unchanged. However, three pronounced modes appeared (Figure 6, underlined wavelengths). The peaks centered at  $3448$  and  $1475\text{ cm}^{-1}$  indicated

the incorporation of  $\text{H}_2\text{O}$ , while the absorption mode at  $1108\text{ cm}^{-1}$  arose due to the formation of corrosion products (Al—O).

Correlative SEM/EDX analysis was applied to identify the role of the IMPs in the corrosion processes at the buried interface. The measurements were performed in situ AFM measurements. Figure 7a shows the SEM images collected in the secondary electron (SE) mode. From the SEM image, it is evident that after 7 h of immersion, most of the IMPs remained in the matrix with minor partial dissolution. Furthermore, the ring-like structures that formed upon collapse of the blisters were also visible in the SEM images (Figure 7a), which were already observed in the AFM topography in Figure 5a. Corresponding EDX measurements identified the elemental composition of these structures as carbon without any indication of enrichment of a certain metallic component, confirming that these are the collapsed parts of the film (Figure 7b). By avoiding the dissolution of the soluble corrosion products into the electrolyte, the presence of the thin model film resulted in the preservation of the interface state after corrosion and a postassignment of the compositions of the IMPs.

Consequently, EDX mapping identified the largest IMPs labeled C and F in Figure 7a as mixtures of either (C) Al—Fe—Mn (Figure 7d,f,g) or (F) Al—Fe—Cu—Mn (Figure 7d—g). The particles labeled E in Figure 7a are identified as the S-phase particles (Al—Cu—Mg) (Figure 7e,g,h). Different from results obtained on bare AA samples, where Mg was selectively dissolved from the S-phase particle after 4 h of corrosion, EDX analysis on coated samples confirmed the presence of Mg within the S-phase particles even after 7 h of corrosion. The Al content within the Fe-containing particles also appeared to be higher than on the uncoated AA sample, which could be explained by the accumulation of the dissolved corrosion products at the polymer/metal interface.

The aim of the correlative analysis was to test the correlation between elemental composition of the surface and the formation and growth of blisters. Figure 8 shows an overlay of the EDX Mg map, as well as the in situ AFM images prepared after 1 and 7 h of corrosion, while a binary image represents the edges (black lines) of the initial blister shape and size after 1 h exposure time.

It is important to note that most of the blisters formed in the vicinity of the Mg particles (pink colored) continued to grow during the corrosion process, while smaller blisters that were further away and only located at the surface of the Al matrix did not change their size significantly.

The use of the model coating has three main effects. First of all, soluble corrosion products cannot escape into the electrolyte. Second, blisters can be viewed as local corrosion cells, which are decoupled from each other in terms of mass transport. This would mean that a redistribution of IMP constituents, for example, Cu redeposition, can only take place within the blister volume. Last but not least, reduction of water generates  $\text{OH}^-$  ions. Considering the rapid growth of the blisters, it is expected that the pH within the blisters will rise immediately. Thus, the role of the pH in confined volumes deserves further attention. As the blister formation was only observed in the vicinity of S-phase particles and on the Al matrix, the discussion of the pH effect will be focused on Al, Cu, and Mg. The main matrix

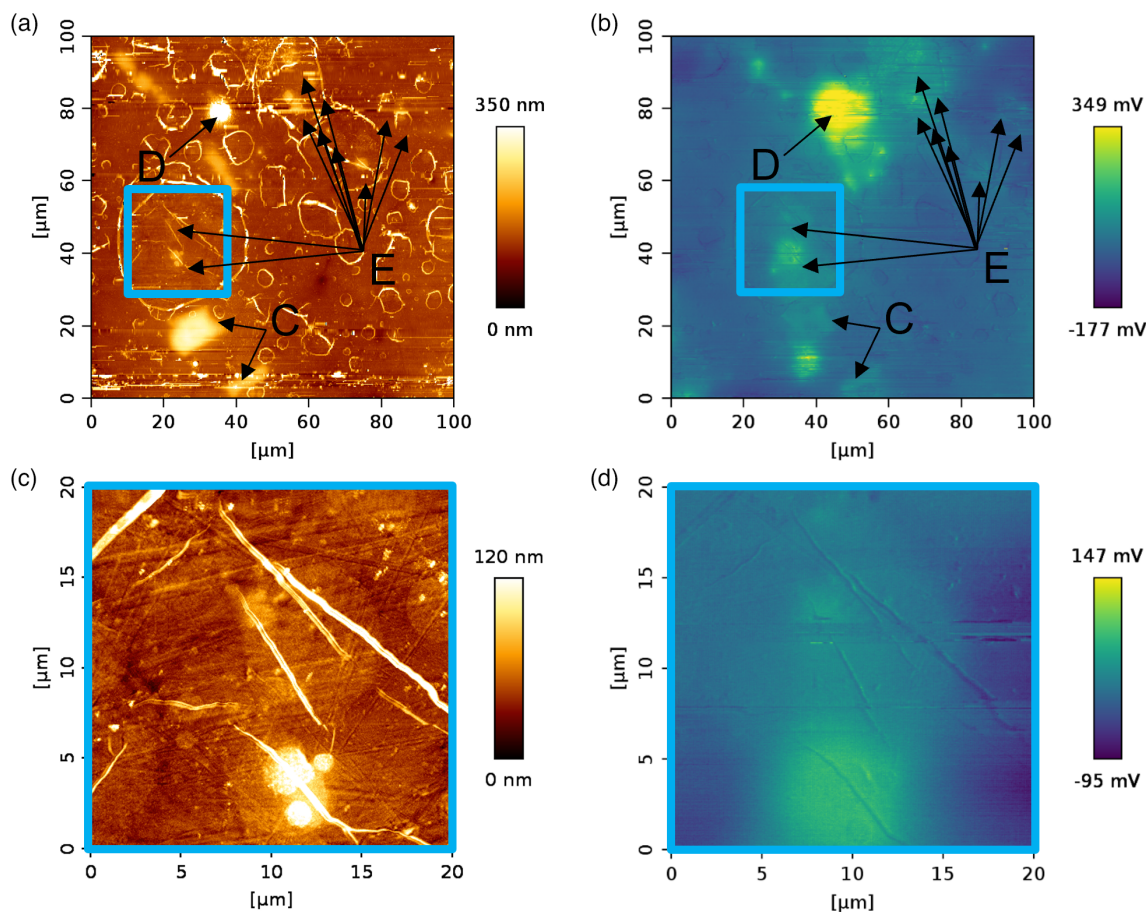


**Figure 5.** a,c) AFM topography images and b,d) Volta potential maps recorded at the surface of (CNER/PEI)<sub>1</sub>/AA a) after in situ AFM corrosion experiments over 7 h in a 0.1 M NaClO<sub>4</sub> electrolyte solution.

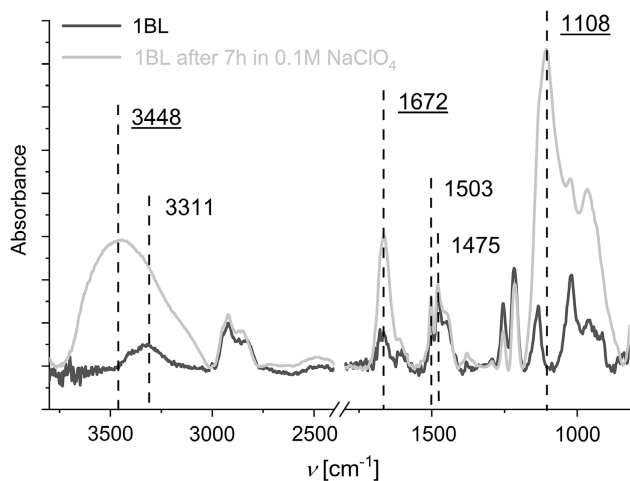


**Figure 6.** FTIR spectra before (black) and after (gray) the in situ AFM corrosion studies at (CNER/PEI)<sub>1</sub>/AA in a spectral range of 4500–800 cm<sup>-1</sup>.

component aluminum shows passivity until pH 8.5–9.0 and may become locally active at higher pH values. Stable copper oxide (Cu<sub>2</sub>O) could form with increasing pH, starting around

pH 9.<sup>[4e]</sup> However, considering that Cu is the most noble constituent of the S-phase IMPs, it is unlikely that Cu will be the driver of the anodic corrosion reaction. The less-noble and most reactive alloy constituent, magnesium, is prone to anodic dissolution until the passivity is reached at pH ≈ 11. Moreover, it was reported by Salleh et al. that the kinetics of hydrogen evolution reaction (HER) is significantly faster on Mg(OH)<sub>2</sub> than on the pristine Mg surface and high pH conditions favoring the growth of Mg(OH)<sub>2</sub>, also supporting HER at higher rates.<sup>[13]</sup> According to Laurent et al., the superfluous hydrogen evolution was evident on bare AA2024-T3 aluminum alloy surfaces during both anodic and cathodic polarization. Moreover, it was promoted by the presence of cathodically active alloying elements within the alloy.<sup>[14]</sup>

Considering that no severe dissolution, dealloying, or trenching was visible on and around the S-phase particles after 7 h of exposure to the electrolyte, the model films can provide an adequate corrosion protection. As the blister growth rate was significantly reduced after the initial phase, it is very likely that an inhibition mechanism exists under these conditions. Such an inhibition effect would also explain the formation of smaller blisters in the beginning of the in situ experiments, mostly in regions where no S-phase IMPs are detected and which do not grow in size at later stages.

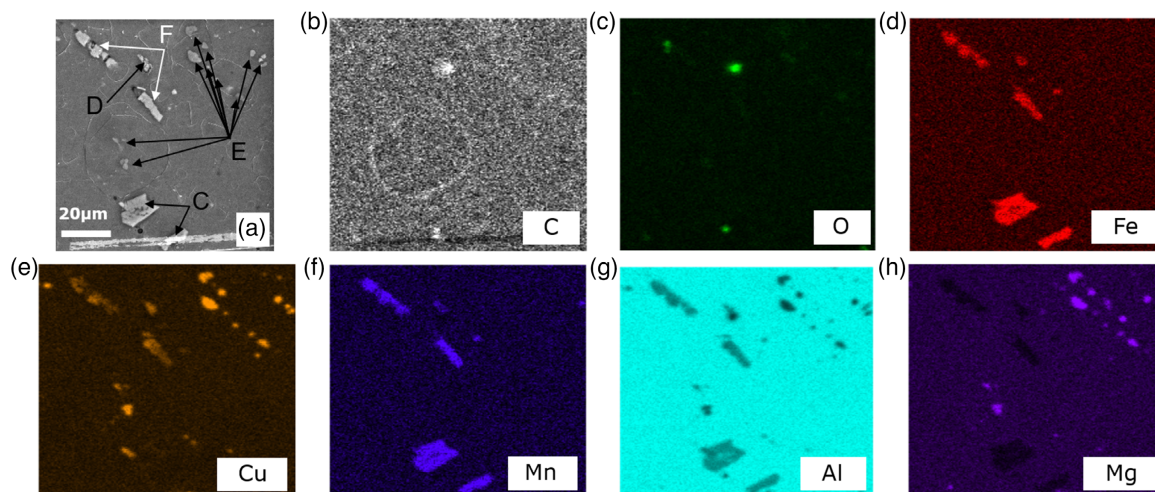


**Figure 7.** a) SEM image recorded in the SE mode and the corresponding EDX analysis showing the presence of b) C, c) O, d) Fe, e) Cu, f) Mn, g) Al, and h) Mg of the same area characterized by AFM.

The FTIR data indicate that the peaks related to the model epoxy-like film did not change after the corrosion experiments. However, vibrations assigned to aluminum oxides and hydroxides dominate the spectra after the in situ AFM measurement series. Even though FTIR spectroscopy does not provide spatially resolved information, the presence of aluminum oxides and hydroxides could explain the observed inhibition effect. The surface area ratio of the S-phase particle and the matrix could be a key factor in determining the extent of the pH increase and thus, whether passivation by deposition of aluminum oxides and hydroxides would be possible. An early onset of passivation and the formation of insulating aluminum oxides would also hinder the HER, undercutting the cathodic corrosion reaction as well.

Unfortunately, the execution of in situ AFM measurements is limited to a certain blister height. Therefore, in situ experiments cannot be prolonged to follow how the blister growth proceeds. In the different series of measurements, the limit was reached at around 5–8 h, depending on the distribution of the IMPs at the measurement area. The clarification of the open questions in this work, especially related to local pH evolution, would require novel analytical tools, for example, the pH-responsive model coatings that can report local pH changes.

It is widely accepted that oxygen reduction is the main cathodic corrosion reaction taking place at the aluminum matrix and nobler Al–Fe–Cu–Mn or Al–Fe–Mn particles on the coated AA2024-T3 aluminum alloy surfaces. Our results indicate that hydrogen reaction at the vicinity of Mg-containing IMPs, probably catalyzed by  $\text{Mg}(\text{OH})_2$  formed on such particles, cannot be overlooked when discussing delamination processes on Mg-containing aluminum alloys. Given the high adhesion strength between the polymeric coating and the alloy surface, water ingress to the interface can lead to blister formation due to HER and detachment of the polymeric coating, leading to delamination processes.

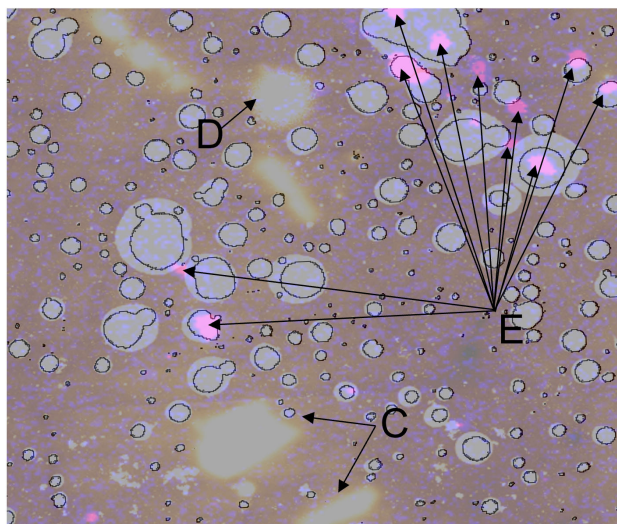


**Figure 8.** Image overlay of the EDX Mg map (Mg components pink colored) and in situ AFM topography after 1 h (binary image representing only the edges of blisters) and 7 h of corrosion (borderless areas). \*The noble IMPs are yellow colored in the layer of the AFM image.

### 3. Conclusion

In situ AFM studies were performed to monitor local corrosion processes at the buried interface between a model epoxy-like thin film and AA2024-T3 aluminum alloy surface in an aqueous 0.1 M  $\text{NaClO}_4$  electrolyte solution. Blister formation was observed in the initial stage of corrosion on coated AA2024-T3 samples due to hydrogen evolution. FTIR results confirmed that the exposure of coated AA2024-T3 samples to the corrosive electrolyte solution does not cause permanent the degradation of the polymer layer, and formation of aluminum oxides and hydroxides as corrosion products was evident.

The SKPFM technique was successfully used to identify the IMPs under the 30 nm-thin model film. After in situ corrosion experiments, a decreased Volta potential difference was observed



between the Fe- and Mg-containing particles and the Al matrix, whereas the overall surface potential was significantly increased. These changes might be associated with the localized dissolution of aluminum matrix around the IMPs and the formation of aluminum oxide/hydroxide.

The correlation between the elemental composition of the aluminum alloy and the formation and growth of blisters at the polymer surface was achieved by means of EDX and in situ AFM studies enabled by the use of the developed thin model organic film. An overlay of the EDX Mg map, as well as the in situ AFM images prepared after 1 and 7 h of corrosion, revealed that the blisters which are growing are located in the vicinity of the Mg-containing IMPs. Our results indicate that the competing cathodic corrosion process at Mg-containing IMPs can play an important role in the degradation of the polymer/alloy interface.

## 4. Experimental Section

**Materials:** Rolled aluminum alloy AA2024-T3 (AA) plates with a nominal composition of 93.5% Al, 4.5% Cu, 1.5% Mg, and 0.5% Mn were purchased from Goodfellow GmbH (Friedberg, Germany). Poly[(*o*-cresyl glycidyl ether)-*co*-formaldehyde] (trade name cresol novolac epoxy resin [CNER], average  $M_n$ :  $\approx 1080 \text{ g mol}^{-1}$ ) and branched poly-(ethylenimine) (PEI, average  $M_w$ :  $\approx 25\,000 \text{ g mol}^{-1}$ ) were purchased from Sigma Aldrich (Steinheim, Germany). Ethanol was obtained from Chemsolute (Berlin, Germany) and  $\text{NaClO}_4$  from PanReac AppliChem IWT Reagents (Darmstadt, Germany). Aqueous solutions were prepared using analytical grade chemicals and deionized water.

**Sample Preparation:** Alloy specimens of dimensions  $20 \times 20 \times 1.6 \text{ mm}$  were cut from the AA plate. The surface of the AA samples was wet ground using silicon carbide papers (ATM GmbH, Germany) up to 4000 grit and further polished with 3 and  $1 \mu\text{m}$  diamond monocrystalline paste (ATM GmbH, Germany), respectively. After each polishing step, the samples were rinsed with deionized water. Finally, AA2024-T3 samples were cleaned in an ultrasonic bath for 5 min in ethanol (98%, Sigma Aldrich, Germany) and dried in an oxygen stream.

**Solutions and Coatings:** CNER was dissolved in chloroform, and PEI solutions were prepared in ethanol, both with a total concentration of 0.2% (w/w). The deposition of the CNER and PEI layers was performed under ambient conditions using SPIN150 wafer spinner (APT GmbH, Germany). A volume of  $400 \mu\text{L}$  was deposited on the supporting surface. Afterwards, the sample was accelerated with  $1000 \text{ rpm s}^{-2}$  to the desired rotation speed of 3000 rpm, where it rotated for 40 s. Finally, the samples were cured at  $80^\circ\text{C}$  for 10 min. The optimization of the coating procedure was described in detail in the study by Almalla et al.<sup>[9]</sup>

**Sample Characterization:** In situ corrosion studies were performed by means of AFM (JPK NanoWizard 4, Bruker Nano GmbH, Berlin, Germany), operating with an image resolution of  $512 \times 512$  pixels. The in situ images were collected in the quantitative imaging (QI) mode with pixel times of 6–18 ms for each pixel using an Cr-/Pt-coated silicon nitride cantilever (Multi75-G tip, Budget Sensors, Canada, USA) with a nominal spring constant of  $75 \text{ N m}^{-1}$ . The operating principle of the QI mode is based on the force spectroscopy imaging mode, where a force distance curve is recorded at each pixel of the image. Retracting the cantilever from the sample surface between each pixel movement prevents lateral forces and allows a better control of vertical forces, which makes this mode very suitable for investigations of the thin polymer layers and the loosely attached corrosion products in aqueous environment. Before and after the in situ corrosion studies, SKPFM was used for characterization of the topography and the Volta potential of the sample surface under ambient conditions. SKPFM imaging was performed in the intermittent mode at a scan frequency of 0.3–0.4 Hz using Cr-/Pt-coated silicon tip (Tap300-G, Budget Sensors, Canada, USA) with a nominal spring constant of  $40 \text{ N m}^{-1}$ . For the determination of the Volta potential, the tip was lifted

by a predefined height of 50 nm while following the topography profile. To initiate the cantilever oscillation, an AC voltage of 1 V was applied to the tip. The detailed operation principles of the SKPFM technique were first described by Nonnenmacher et al.<sup>[15]</sup> As no absolute reference was used in SKPFM analysis, the reported values in this study were potential differences. As imaging in the intermittent mode proved to be challenging after the in situ AFM corrosion studies, the QI mode was used to obtain better quality of the topography profiles. The software JPK Data Processing 6.1.88 was used for offline analysis of the topography and film thickness. Image flattening was performed with the first-order, least-square polynomial function, which removes the tilt and the vertical z-offset between line scans. A VEGA3 TESCAN system equipped with an EDX detector operated at 20 kV was used to record all the scanning electron microscopy (SEM) images and EDX data.

## Acknowledgements

The authors would like to thank Michaela Buchheim for the scanning electron microscopy and energy-dispersive X-ray spectroscopy measurements. Open access funding enabled and organized by Projekt DEAL.

## Conflict of Interest

The authors declare no conflict of interest.

## Data Availability Statement

The data that support the findings of this study are available from the corresponding author upon reasonable request.

## Keywords

aluminum alloys, buried interfaces, in situ atomic force microscopy, local corrosion, scanning Kelvin probe force microscopy

Received: September 30, 2021

Revised: December 20, 2021

Published online:

- [1] a) J. E. Hatch in *Properties of Pure Aluminium* (Ed. J. E. Hatch), American Society for Metals, Metals Park, Ohio, USA, **1984**; b) A. Boag, A. E. Hughes, A. M. Glenn, T. H. Muster, D. McCulloch, *Corros. Sci.* **2011**, *53*, 17; c) Z. Huda, N. I. Taib, T. Zaharinie, *Mater. Chem. Phys.* **2009**, *113*, 515.
- [2] a) R. G. Buchheit, R. P. Grant, P. F. Hlava, B. McKenzie, G. L. Zender, *J. Electrochem. Soc.* **1997**, *144*, 2621; b) N. Birbilis, R. G. Buchheit, *J. Electrochem. Soc.* **2005**, *152*, B140; c) R. G. Buchheit, *J. Electrochem. Soc.* **1995**, *142*, 3994; d) A. Kosari, F. Tichelaar, P. Visser, H. Zandbergen, H. Terry, J. M. C. Mol, *Corros. Sci.* **2020**, *177*, 108947; e) M. Olgiati, P. J. Denissen, S. J. Garcia, *Corros. Sci.* **2021**, *192*, 109836.
- [3] a) N. R. Cawley, D. G. Harlow, *J. Mater. Sci.* **1996**, *31*, 5127; b) C. Blanc, B. Lavelle, G. Mankowski, *Corros. Sci.* **1997**, *39*, 495; c) A. Boag, R. J. Taylor, T. H. Muster, N. Goodman, D. McCulloch, C. Ryan, B. Rout, D. Jamieson, A. E. Hughes, *Corros. Sci.* **2010**, *52*, 90; d) E. Hughes Anthony, R. Parvizi, M. Forsyth, *Corros. Rev.* **2015**, *33*, 1.
- [4] a) S. Malladi, C. Shen, Q. Xu, T. de Kruijff, E. Yucelen, F. Tichelaar, H. Zandbergen, *Chem. Commun.* **2013**, *49*, 10859; b) V. Guillaumin, P. Schmutz, G. S. Frankel, *J. Electrochem. Soc.* **2001**, *148*, B163;

- c) P. Schmutz, G. S. Frankel, *J. Electrochem. Soc.* **1998**, *145*, 2285; d) P. Schmutz, G. S. Frankel, *J. Electrochem. Soc.* **1998**, *145*, 2295; e) B. Zhang, J. Wang, B. Wu, E. E. Oguzie, K. Luo, X. L. Ma, *Sci. Rep.* **2016**, *6*, 39525; f) J. Wang, B. Zhang, Y. T. Zhou, X. L. Ma, *Acta Mater.* **2015**, *82*, 22; g) A. Kosari, H. Zandbergen, F. Tichelaar, P. Visser, P. Taheri, H. Terryn, J. M. C. Mol, *Corros. Sci.* **2020**, *177*, 108912.
- [5] P. Leblanc, G. S. Frankel, *J. Electrochem. Soc.* **2002**, *149*, B239.
- [6] a) C. Senöz, M. Rohwerder, *Electrochim. Acta* **2011**, *56*, 9588; b) P. P. Leblanc, G. S. Frankel, *J. Electrochem. Soc.* **2004**, *151*, B105; c) F. P. Yang, Z. Jiang, Q. M. He, Z. M. Zhang, Y. Zhou, E. Karapetrova, M. D. Soucek, M. D. Foster, *ACS Appl. Mater. Interfaces* **2019**, *11*, 3555; d) S. Pletincx, L. Trotochaud, L. L. Fockaert, J. M. C. Mol, A. R. Head, O. Karslıoglu, H. Bluhm, H. Terryn, T. Hauffman, *Sci. Rep.* **2017**, *7*, 45123.
- [7] C. Senoz, S. Borodin, M. Stratmann, M. Rohwerder, *Corros. Sci.* **2012**, *58*, 307.
- [8] a) M. Rohwerder, F. Turcu, *Electrochim. Acta* **2007**, *53*, 290; b) M. Rohwerder, E. Hornung, M. Stratmann, *Electrochim. Acta* **2003**, *48*, 1235.
- [9] A. Almalla, A. Hertwig, D. Fischer, O. Ozcan, J. Witt, *J. Appl. Polym. Sci.* **2020**, *137*, 49826.
- [10] Y. K. Zhu, K. Sun, G. S. Frankel, *J. Electrochem. Soc.* **2018**, *165*, C807.
- [11] Y. Zhai, S. S. C. Chuang, *Ind. Eng. Chem. Res.* **2017**, *56*, 13766.
- [12] W. Choi, K. Min, C. Kim, Y. S. Ko, J. W. Jeon, H. Seo, Y.-K. Park, M. Choi, *Nat. Commun.* **2016**, *7*, 12640.
- [13] a) S. H. Salleh, S. Thomas, J. A. Yuwono, K. Venkatesan, N. Birbilis, *Electrochim. Acta* **2015**, *161*, 144; b) M. Esmaily, J. E. Svensson, S. Fajardo, N. Birbilis, G. S. Frankel, S. Virtanen, R. Arrabal, S. Thomas, L. G. Johansson, *Prog. Mater. Sci.* **2017**, *89*, 92.
- [14] C. Laurent, F. Scenini, T. Monetta, F. Bellucci, M. Curioni, *Npj Mater. Degrad.* **2017**, *1*, 6.
- [15] M. Nonnenmacher, M. P. Oboyle, H. K. Wickramasinghe, *Appl. Phys. Lett.* **1991**, *58*, 2921.